Sol–gel synthesis of $Cu_{0.9}Zn_{0.05}M_{0.05}O$ (M = Cr, Co, Cd) nanocrystals for removal of pollutant dyes and bacterial inactivation

Tauseef Munawar[1], Muhammad Shahid Nadeem[1], Muhammad Naveed ur Rehman[1], Faisal Mukhtar[1], Muhammad Riaz[1], and Faisal Iqbal[1,*] (ID)

[1] Institute of Physics, The Islamia University of Bahawalpur, Bahawalpur 63100, Pakistan

ABSTRACT

In this work, we focus on the synthesis of $Cu_{0.95}Zn_{0.05}O$ and $Cu_{0.9}Zn_{0.05}M_{0.05}O$ (M = Cr, Co, Cd) nanocrystals by employing low-cost sol–gel method. The effect of single doping and co-doping on physical, antibacterial, and photocatalytic properties of CuO has been successfully investigated using characterization tools comprising XRD, SEM, FTIR, UV–Vis, and I–V measurements. X-ray diffraction pattern exhibited that the grown product of CuO has no traces of impurities, indicated the successful incorporation of dopants without changing monoclinic structure. The X-ray peak profile analysis was adopted to calculate the average crystallite size (D) by considering the contributions of lattice strain on peak broadening. The calculated direct energy bandgap indicated redshift (1.26 eV to 1.81) eV by co-doping. The I–V study revealed the enhancement in electrical properties by co-doping. The effects of co-doping on photocatalytic properties of CuO were studied by degradation of methylene blue (MB) and methyl orange (MO) dyes under direct sunlight. The Zn/Cd-doped nanocrystal has a higher degradation efficiency 98.4% against MB and 96.1% against MO dye in 50 min. The enhanced photodegradation is due to the generation of reactive species confirmed by scavenger's experiments. The recyclability test showed the reusability of grown catalyst up to the 4th cycle. The antibacterial property was studied against *Staphylococcus aureus* and *Klebsiella pneumoniae* bacterial strains, which showed the highest zone of inhibition 31 mm, and 32 mm for co-doped samples. Furthermore, the present study paves the path to modify the properties of CuO for optoelectronic devices, environmental, and biomedical applications.

Address correspondence to E-mail: faisal.iqbal@iub.edu.pk

Springer

1 Introduction

Nowadays, nanotechnology is a diverse field for fabricating nanometer-scale materials having multifunctional applications, such as catalysts, biomedical, and environmental science, etc. [1, 2]. The ever-increasing in industrial development is the primary cause of an increase in global environmental pollution [3, 4]. The disposal from the textile industry includes dyestuffs, and harmful gases or liquids are the pivotal issues worldwide for human society [5–7]. The different physicochemical techniques have been employed to eliminate the harmful effects of these carcinogenic dyes, including biological and chemical treatments [8]. Among them, photocatalysis is a promising method for the complete removal of synthetic dyes from wastewater [9–14]. Heterogeneous photocatalysis encompassing metal oxide semiconductors has appeared as a favorable method because it required solar energy, which is readily available almost every part of the earth. Metal oxide semiconductors having exceptional features, such as their chemical stability, cost effective, and less toxicity, which made them beneficial for practical application [15, 16]. Nowadays, different microorganisms have been detected in the world due to an increase in habitat and food items. Most of these microorganisms are favorable for breathing organisms, environment as well as human beings. In spite of these valuable microorganisms, some are dangerous, causing severe health issues by spreading diseases, known as pathogens. It is crucial to investigate innovative drugs or materials with an extensive spectrum of significant antimicrobial activities. As there is a gradual development in different antibiotic-resistant bacterial strains as well as to develop novel delivery and targeting strategies [17]. In comparison with the acceleration in antibiotic resistance, there is the scarcity of new antimicrobials agents. Nanomaterials, like metallic and metal oxide nanoparticles (NPs), can elicit promising and potent role as antimicrobial agents.

Among various available semiconductor metal oxides, CuO is an earth-abundant compound that has gained remarkable attention due to its low energy gap of 1.2 eV in the visible region [18]. CuO crystallizes with a monoclinic structure having n-type semiconductor behavior. It possesses excellent physical and chemical properties. It is comparatively nontoxic and inexpensive material [19]. It is effectively used in magnetic storage media, solar cells, bioimaging, environmental remediation, antibacterial agent, superconductor, anti-inflammatory activity, sensing material, ceramics, and photovoltaics/optoelectronic devices, etc. [20–23].

Recently, researchers have made a lot of efforts to modify structural, optical, and photocatalytic properties of CuO with doping transition-metal-ions (TM). Apart from different transition metals (TM) elements, zinc (Zn), chromium (Cr), cobalt (Co), and cadmium (Cd) have great potential for enhancing its physical properties and tuning the energy bandgap. Different studies are available about the doping of Zn, Cr, Co, and Cd in CuO. Gedanken et al. [24] have synthesized Zn-doped CuO and reported the enhanced antioxidant detection and glucose sensitivity by Zn–CuO nanoparticles. Anu et al. [25] have synthesized Zn-doped CuO nanoparticles by the microwave-assisted method and investigated the structural and morphological properties of Zn–CuO nanoparticles. Sun et al. [26] have synthesized Co-doped CuO nanoarray electrocatalyst by wet chemical reaction. They reported superior durability up to 15 h by Co–CuO electrocatalyst with 0.056 mol O2 s^{-1} turnover frequency at 300 mV potential. The improved properties of CuO by transition-metal-ions (TM) doping have been reported, but the combined effect of M = (Cr, Co, Cd) and Zn co-doping in CuO could not be found. El Sayed et al. [27] have synthesized Co, Fe co-doped CuO thin film and reported enhanced photocatalytic performance against MB dye. They also have reported the redshift in energy gap and modification in structure by incorporation of Co and Fe in CuO. Mohamed Shaban et al. [28] have synthesized Cr + S-doped CuO thin film and reported the improvement in structural and optical properties along with enhancement in the gas sensing properties.

The influence of single (Cr, Co, and Cd) transition metal doping in CuO is reported, but there is no report to study the effects of co-doping of Zn along with Cr, Co, and Cd in the CuO host matrix. With this background, the structural, energy gap, and photocatalytic properties of CuO was investigated by co-doping with M = (Cr, Co, Cd) and Zn. The co-doping of these transition elements may cause a drastic change and improvement in the physical properties of CuO. In this perspective, $Cu_{0.95}Zn_{0.05}O$ and $Cu_{0.9}Zn_{0.05}M_{0.05}O$ (M = Cr, Co, Cd) samples may attract remarkable attention.

Several methods have been used for the synthesis of metal oxide nanostructure, including sol–gel, hydrothermal, microwave-assisted, ultra-sonic-assisted, and homogeneous co-precipitation methods [29–32]. Among these, the sol–gel method is a simple, effective, low-temperature, and low-cost process [33].

In this study, we focus on the synthesis of $Cu_{0.95}Zn_{0.05}O$ and $Cu_{0.9}Zn_{0.05}M_{0.05}O$ (M = Cr, Co, Cd) nanocrystals using sol–gel method. XRD, SEM, FTIR, UV–Vis, and I–V measurements are used to study the properties of grown nanocrystals. The X-ray peak profile analysis was performed using Scherrer, W–H, and SSP methods to calculate the average crystallite size (D) and lattice strain by considering the contributions of the X-ray peak broadening effect. The direct energy bandgap was estimated by UV–Vis spectra. The variation in electrical properties by the co-doping were studied by I–V measurements. The effects of Zn doping and Zn & M (M = Cr, Co, Cd) co-doping on photocatalytic properties of CuO were also studied against MB and MO dyes under direct sunlight. The antibacterial property was studied against *Staphylococcus aureus* and *Klebsiella pneumoniae* bacterial strains.
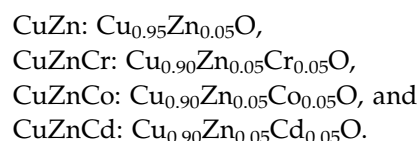
2 Experimental

2.1 Materials

The source material was copper acetate monohydrate ($Cu(CH_3COO)_2 \cdot H_2O$), while zinc acetate dihydrate ($Zn(CH_3COO)_2 \cdot 2H_2O$), cadmium nitrate hexahydrate ($Cd(NO_3)_2 \cdot 6H_2O$), cobalt nitrate hexahydrate ($Co(NO_3)_2 \cdot 6H_2O$), and chromium nitrate hexahydrate ($Cr(NO_3)_3 \cdot 6H_2O$) were used as a dopant material, and methylene blue (MB) and methyl orange (MO) dyes were used as organic pollutants. The NaOH was used as a precipitating agent. Distilled water and ethanol (C_2H_5OH) were used for washing. All chemicals from a commercial source (Sigma-Aldrich) were used as received without further purification.

2.2 Preparation of nanocrystals

For the preparation of Zn-doped CuO, 0.1 M of each salt of copper acetate monohydrate and zinc acetate dihydrate were mixed in distilled water and vigorously stirred for 30 min for complete dissolution. The 0.1 M aqueous NaOH was added dropwise keeping constant stirring until pH 9. The obtained solution was stirred at 70 °C for 3 h to obtain the gel. The obtained gel was dried at 80 °C for 2 h and finally annealed at 650 °C for 2 h. The same experimental procedure is used to synthesize all co-doped nanocrystals by taking an appropriate amount of 0.1 M of dopant salts and copper salt. The obtained products were named as follows:

CuZn: $Cu_{0.95}Zn_{0.05}O$,
CuZnCr: $Cu_{0.90}Zn_{0.05}Cr_{0.05}O$,
CuZnCo: $Cu_{0.90}Zn_{0.05}Co_{0.05}O$, and
CuZnCd: $Cu_{0.90}Zn_{0.05}Cd_{0.05}O$.

2.3 Photocatalytic test

The photocatalytic characteristics of the as-synthesized catalysts was studied using direct sunlight using MB and MO dyes as model pollutants. At the start, 20 mg of the grown photocatalysts was suspended in a 50 ml solution of dyes in eight separate beakers at fixed concentrations of dye (5 ppm). First, catalyst/dye solutions are magnetically stirred in a dark environment for 1 h until the adsorption–desorption equilibrium was established, then exposed to sunlight. At different time intervals of irradiation, 5 ml of the solution was extracted. The extracted solution was centrifuged at 6000 rpm for 10 min to eliminate catalyst particles and analyzed by UV–Vis spectrometer. The degradation efficiency of pollutants was calculated using the following equation [34, 35]:

$$\text{Degradation efficiency } (\eta) = [(C_o - C_t)/C_o] \times 100\% \tag{1}$$

where C_o and C_t are the initial and final absorbance (at different times). Moreover, the species trapping experiments were also performed to investigate the degradation mechanism using different scavengers, including $AgNO_3$, isopropanol (IPA), EDTA-2Na, and ASC, against MB dye.

2.4 Antibacterial test

For antibacterial test, different bacterial culture plates were produced from old culture plates for each strain, maintained on Luria broth (LB) medium, and absorbance of starter cultures was ascertained spectrophotometrically at 600 nm. Different concentrations of the synthesized nanocrystals were tested for
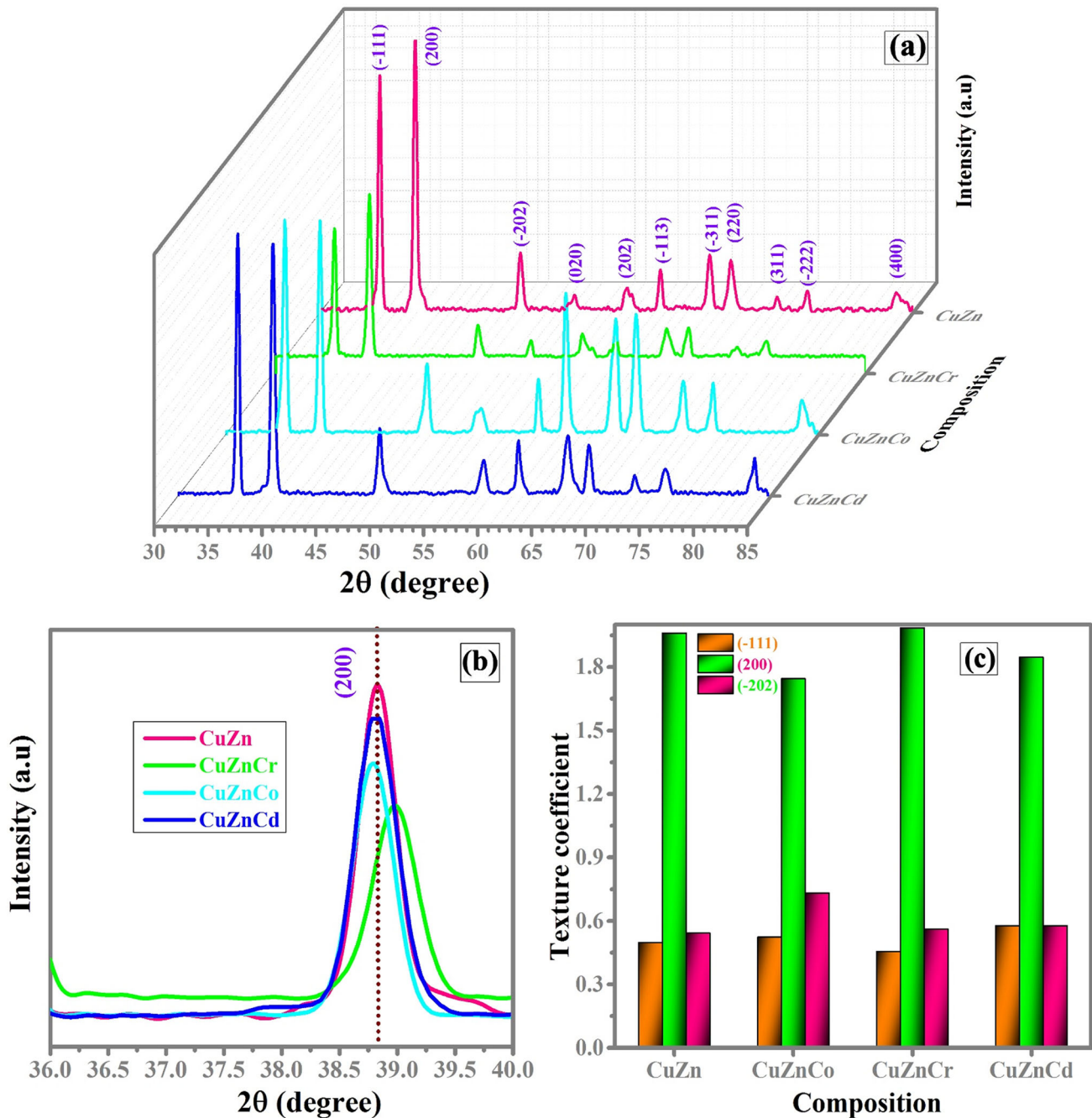
Fig. 1 **a** X-ray diffraction patterns of grown nanocrystals, **b** peak shifting of (2 0 0) plane, and **c** texture coefficient ($TC_{(hkl)}$) for prominent peaks

bacterial activity against Staphylococcus aureus and Klebsiella pneumonia. A stock solution of different concentrations at 1 µg/m, 2 µg/m, and 4 µg/ml with a control of standard drug ciprofloxacin was prepared in distilled water along with disk soaked in this nanocrystals solution. A 20 ml of 2.8–3 g nutrient agar was poured into the Petri plate and then 150 µl of particular bacteria was swabbed on the solidified agar. After distributing of bacterial culture on dish, the disk was placed on the plate with a determined concentration sign and incubated for 24 h at 37 °C, and then the ZOI (zone of inhibition) is measured.

Table 1 Structural parameters of grown samples

Samples	a (Å)	b (Å)	c (Å)	Volume (Å³)	Bond length (Å)	Beta (Å)	d-spacing (Å)	V (10^3 nm³)	Nu (10^6)
CuZn	4.69478	3.41877	5.08743	80.2110	1.82	100.79182	1.78688	29.791	371.41
CuZnCr	4.68627	3.39183	5.09699	79.6100	1.80	100.69313	1.77484	35.937	451.41
CuZnCo	4.68981	3.42721	5.09262	80.4897	1.81	100.47322	1.84479	32.768	407.11
CuZnCd	4.67723	3.42311	5.13602	81.0632	1.79	99.66803	1.79716	39.304	484.87

2.5 Characterization

The structural analysis is performed by X-ray diffractometer (Bruker-D8, $CuK\alpha$ radiation with $\lambda = 1.5406$ Å, range of $2\theta = 30°–85°$) and FTIR Spectrometer (Bruker Tensor 27, range 400–4000 cm^{-1}).

The absorption was traced by a UV–Vis spectrophotometer from 400 to 1250 nm (Cary-60 Agilent Technologies). The I–V measurements (Keithley picometer 6487) were carried out for electrical analysis. The surface morphology was investigated by using Scanning Electron Microscope (Emcrafts cube 2020).
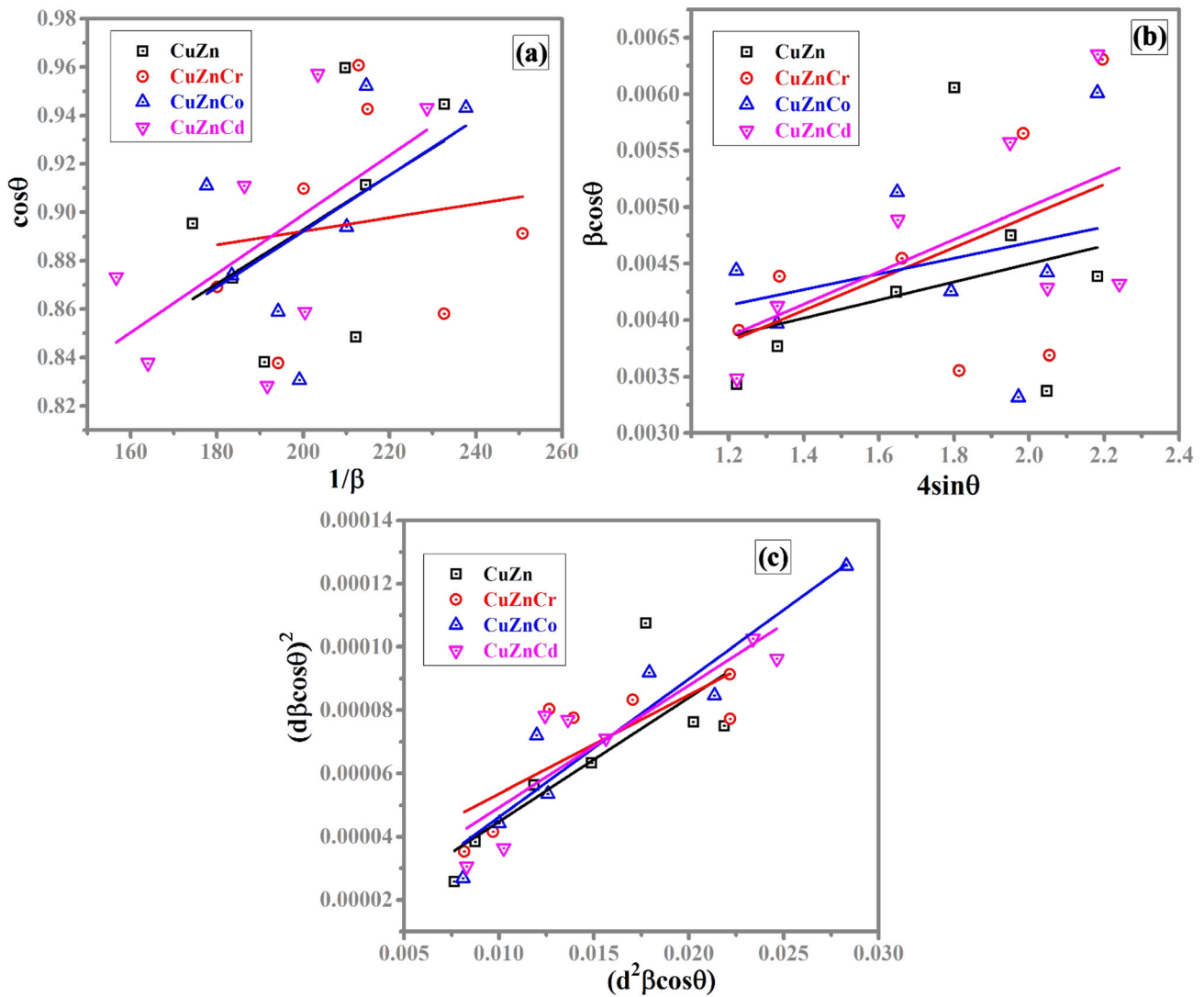

Fig. 2 **a** Scherrer, **b** W–H, and **c** SSP plots

3 Results and discussion

3.1 X-ray analysis

XRD diffraction is an ideal tool for structural analysis and phase composition investigation. Figure 1a shows the XRD characteristic diffraction peaks of grown $Cu_{0.95}Zn_{0.05}O$ and $Cu_{0.9}Zn_{0.05}M_{0.05}O$ (M = Cr, Co, Cd) nanocrystals. The observed peaks are well matched with standards peaks and evidenced the preparation of required products are successfully done. Black-colored powder of Zn-doped and Zn-M (M = Cr, Co, Cd) co-doped CuO nanocrystals is obtained, and all visualized characteristics diffraction peaks correspond to CuO (space group: C2/c; JCPDS 00-005-0661; phase = monoclinic). No other peaks of Zn, Cr, Co, and Cd oxides or hydroxides are found in the XRD pattern which specifies that dopants are successfully incorporated in the CuO matrix or uniformly substitute at Cu^{2+} sites. The structural parameters, including lattice constant (a,b,c), angle (β), d-spacing, the volume of the unit cell (v), bond length (l), the volume of crystallite (V), and number of the unit cell (N_u), are calculated, and the values are summarized in Table 1 [36, 37].

For all grown products of different dopants, the following variations have been perceived. The structural parameters were decreased for CuZnCr and peaks shifted toward higher angle theta as compared to CuZnCo and CuZnCd and peaks shifted toward lower angle theta as compared to CuZn nanocrystal, as observed in Fig. 1b. The cause of this behavior is the difference in atomic radii of Cu (0.72 Å) and dopants Zn (0.74 Å), Cr (0.52 Å), Co (0.74 Å), and Cd (0.95 Å) [27, 38, 39]. The peak shifting toward lower or higher angle theta is due to the doping of larger/smaller ionic radius, which affects the d-spacing of crystallographic planes. The variation in lattice
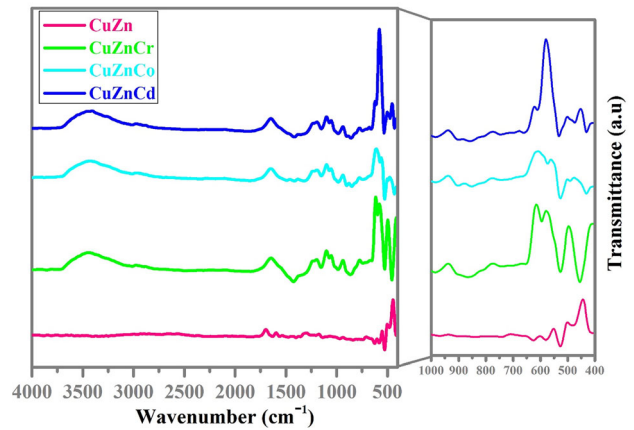

Fig. 3 FTIR spectra of **a** CuZn, **b** CuZnCr, **c** CuZnCo, and **d** CuZnCd nanocrystals

parameters of the host material due to the incorporation or substitution of dopants or foreign atoms has already been reported by different researchers [40–44]. In this perspective, the above results confirmed the successful incorporation or uniform substitution of dopants elements in the host CuO lattice. The crystallite orientations can be studied by texture coefficient ($TC_{(hkl)}$) and its value can be calculated using the following equation [45]:

$$TC_{(hkl)} = \frac{I_{(hkl)}/I_{o(hkl)}}{\left(\frac{1}{N}\right)I_{(hkl)}/I_{o(hkl)}} \tag{2}$$

where $I_{o(hkl)}$, $I_{(hkl)}$, and N are the intensity taken from the XRD pattern, the standard intensity (from JCPDS card), and total no. of peaks, respectively. The texture coefficient for (− 111), (200), and (− 202) planes are illustrated in Fig. 1c. It can also be observed in Fig. 1c that a single-doped (Zn) and co-doped [(Zn + Cr), (Zn + Co), and (Zn + Cd)] CuO samples have a variation in crystalline orientation. The texture coefficient ($TC_{(hkl)}$) is greater than one for the planes (200)

Table 2 Microstructural parameters calculated from Scherrer, W-Hall, and SSP methods

Samples	Scherrer method	Scherrer plot method	Williamson-Hall method		Size-strain plot method		Dislocation density δ $(nm)^{-2} \times 10^{-4}$
	D (nm)	D (nm)	D (nm)	ε ($\times 10^{-4}$)	D (nm)	ε ($\times 10^{-3}$)	
CuZn	31	48	50	8.02	37	4.74	8.68
CuZnCr	32	72	68	1.39	46	9.45	9.24
CuZnCo	33	45	44	6.95	33	3.19	9.12
CuZnCd	34	69	56	1.43	38	6.54	9.91

Table 3 Vibrational parameters calculated from FTIR data

Oxides	Wave number (cm^{-1})	Effective mass (10^{-26} kg)	Force constant, k (N/cm)	Bond length (Å)	Optical phonon frequency, v_o (Hz) 10^{13}	Debye temperature, θ_D (K)
CuZn	578	2.1223	2.5192	1.8897	1.734	833
CuZnCr	596	–	2.6785	1.8515	1.788	858
CuZnCo	574	–	2.4845	1.8985	1.722	827
CuZnCd	532	–	2.1343	1.9971	1.596	766

for all samples, reveals the good growth along this plane.

3.1.1 Microstructural parameters

The physical properties of nanocrystals can be altered by the variations in crystallite size and micro-strain, as there is no perfect crystal due to its finite size [46]. A small change in crystallite size (D) and the micro-strain (ε) due to dislocation or imperfection can be studied by X-ray peak broadening. X-ray profile analysis is used to study the change in microstructural quantities (crystalline size and strain) using various analytical methods, including Scherrer, W–H, and SSP [47, 48]. The crystallite size is calculated by Scherrer's formula [49]:

$$D = \frac{K\lambda}{\beta_D \cos \theta} \tag{3}$$

where D is the crystalline size, λ is the wavelength of X-rays, k is the shape factor (= 0.94), β_D is the FWHM relates with instrument broadening, and θ is the Bragg's angle. The breadth of diffraction peaks includes both the sample and instrumental broadening as

$$\beta_{hkl} = \beta_D + \beta_s \tag{4}$$

where β_{hkl} is the total peak broadening and β_s is the FWHM associated with line broadening.

Rearranging Eq. (3),

$$D = \frac{K\lambda}{\beta_D \cos \theta} = > \cos \theta = \frac{K\lambda}{D}\left(\frac{1}{\beta_D}\right) \tag{5}$$

The term $1/\beta_D$ is drawn versus $\cos\theta$ and linearly fit the data (Fig. 2a); the D was calculated from the slope. The Williamson–Hall UDM model, which considered the uniform micro-strain, is given as [50]

$$\beta_{hkl} = \frac{k\lambda}{D \cos \theta} + 4\varepsilon \tan \theta \tag{6}$$
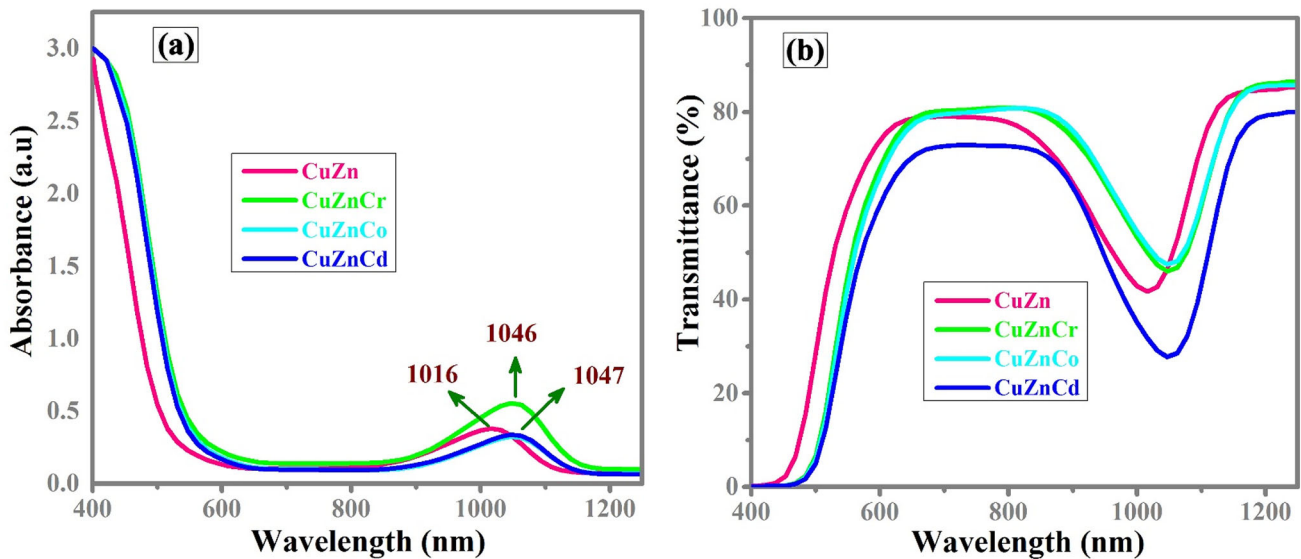
By rearranging Eq. (6),

Fig. 4 Variation of **a** absorbance and **b** transmittance, with incident photon wavelength
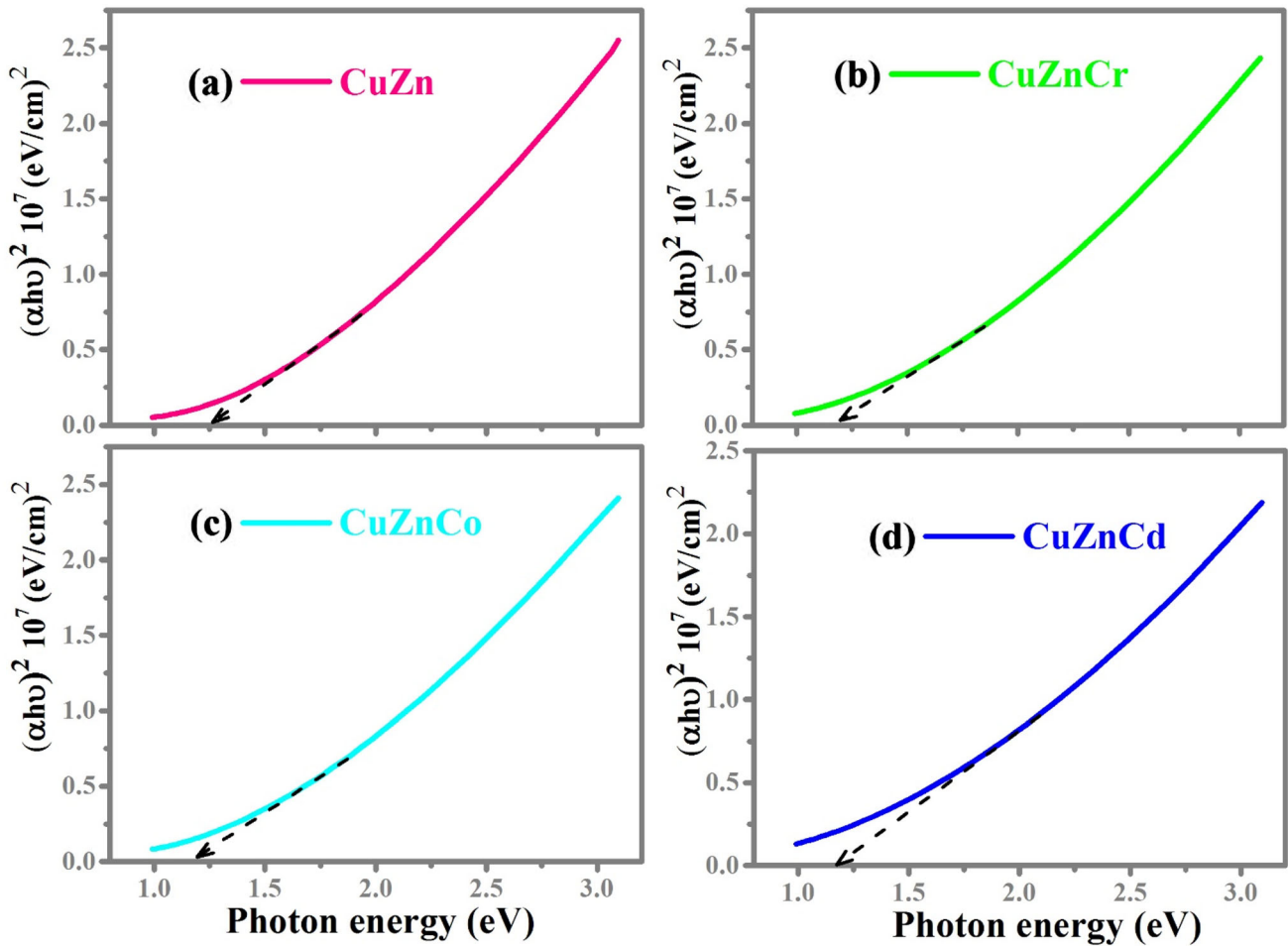
Fig. 5 Tauc's plot for **a** CuZn, **b** CuZnCr, **c** CuZnCo, and **d** CuZnCd nanocrystals

$$\beta_{hkl} \cos \theta = \frac{k\lambda}{D} + 4\varepsilon \sin \theta \qquad (7)$$

The plot of the term $\beta_{hkl} \cos\theta$ *vs* $4\sin\theta$ is drawn (see Fig. 2b), the D is calculated from the y-intercept, and micro-strain is extracted from the slope. The size–strain equation is given as [51]

$$(d_{hkl}\beta_{hkl} \cos \theta)^2 = \left(\frac{k}{D}\right)d_{hkl}^2\beta_{hkl} \cos \theta + \left(\frac{\varepsilon}{2}\right)^2 \qquad (8)$$

The plot of term $d^2_{hkl}\beta_{hkl} \cos\theta$ *vs* $(d_{hkl}\beta_{hkl}\cos\theta)^2$ is drawn (Fig. 2c), the D is calculated from the slope, and strain is extracted from the intercept.

The calculated values of all structural parameters are summarized in Table 2, which indicates that the crystallite size is increased by co-doping. The dislocation density is calculated using equation $\delta = 1/D^2$, which showed an opposite trend from crystallite size as it has an inverse relation with crystallite size. From the obtained results of all the above discussed
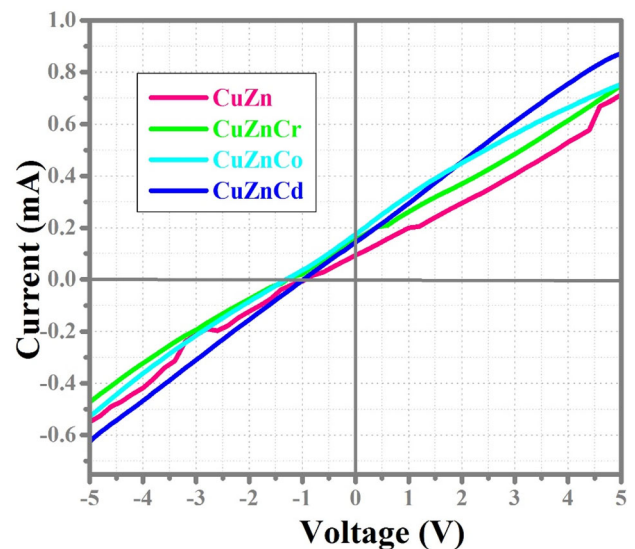

Fig. 6 *I–V* curves of all grown nanocrystals

methods, it is concluded that the size–strain method is more reliable because maximum linear fitting is achieved with more number of data points touching the fitted line.

3.2 FTIR analysis

The study of FTIR is supreme for functional group identification and the analysis of inter/intramolecular interactions. Figure 3 shows the spectra of CuZn, CuZnCr, CuZnCo, and CuZnCd nanocrystals. The noticeable vibrational peaks between 400 and 700 cm^{-1} are attributed to Cu–O bond, while from 700 to 800 cm^{-1} are due to Cu–M–O (M = Zn, Cr, Co, and Cd) lattice vibrations [52, 53]. The existence of additional bands are due to the bonding with

dopants ions, further confirmed the uniform substitution of incorporation of Zn, Cr, Co, and Cd ions in the CuO matrix. The other peaks from 800 to 1000 cm^{-1} are correspond to C–OH group vibration. The absorption bands from 1000 to 1700 cm^{-1} are relating to the stretching vibration of the − COOH acetate group and the C–O group [54]. Additionally, to aid the FTIR analysis, some other physical parameters, including effective mass (μ), force constant (k), bond length (l) of the Cu–O bond, optical phonon frequency (v_o), and Debye temperature θ_D, are calculated using the following relations [55, 56]:

$$\mu = m_1 \times m_2/m_1 + m_2 \qquad (9)$$

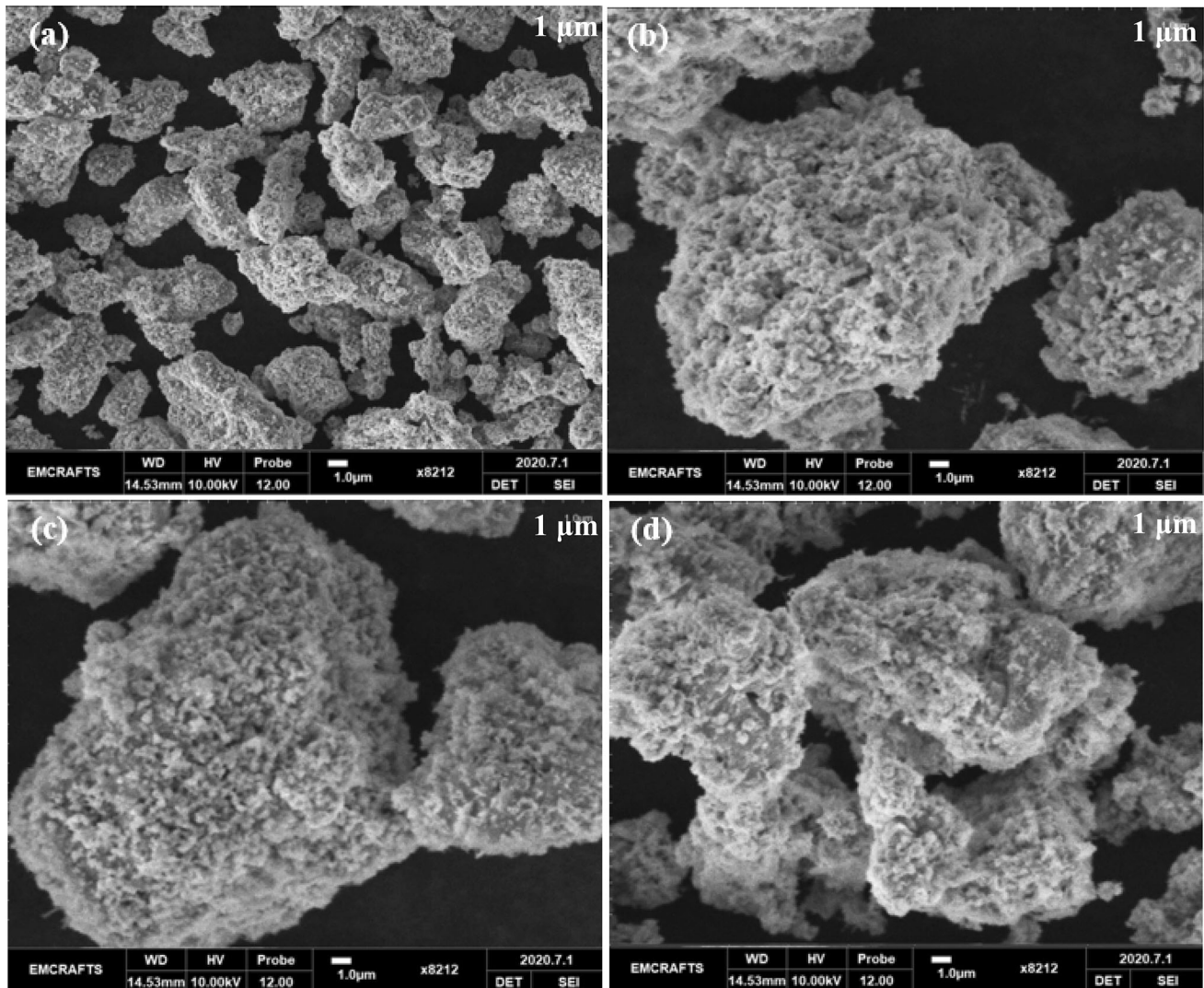$$\bar{v} = (1/2\pi c)\sqrt{k/\mu} \qquad (10)$$

Fig. 7 SEM images of **a** CuZn, **b** CuZnCr, **c** CuZnCo, and **d** CuZnCd nanocrystals
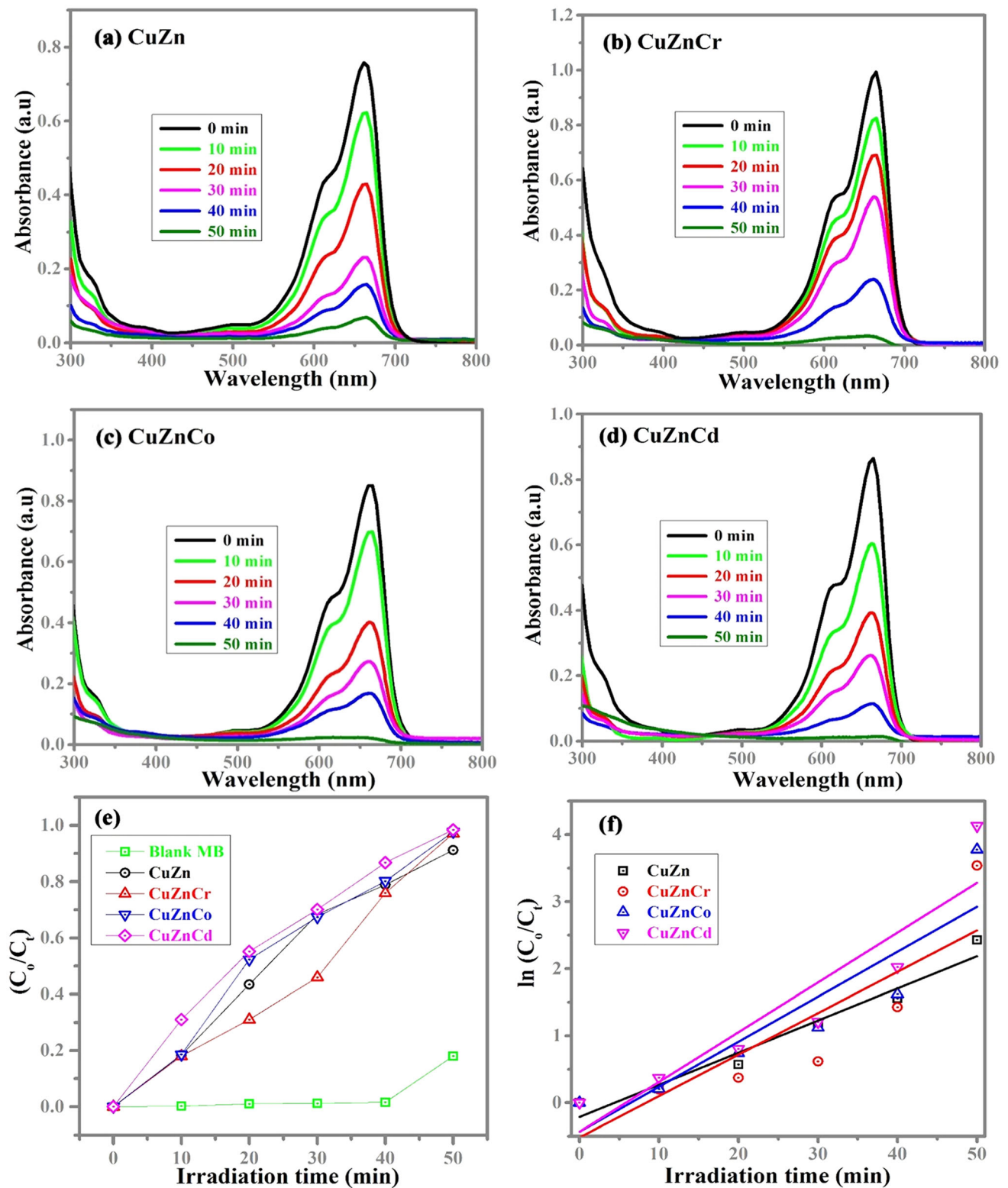
Fig. 8 Absorption spectra of methylene blue (MB) dye in the presence of **a** CuZn, **b** CuZnCr, **c** CuZnCo, **d** CuZnCd photocatalyst, **e** % age degradation, and **f** kinetic plot for rate constant (k)
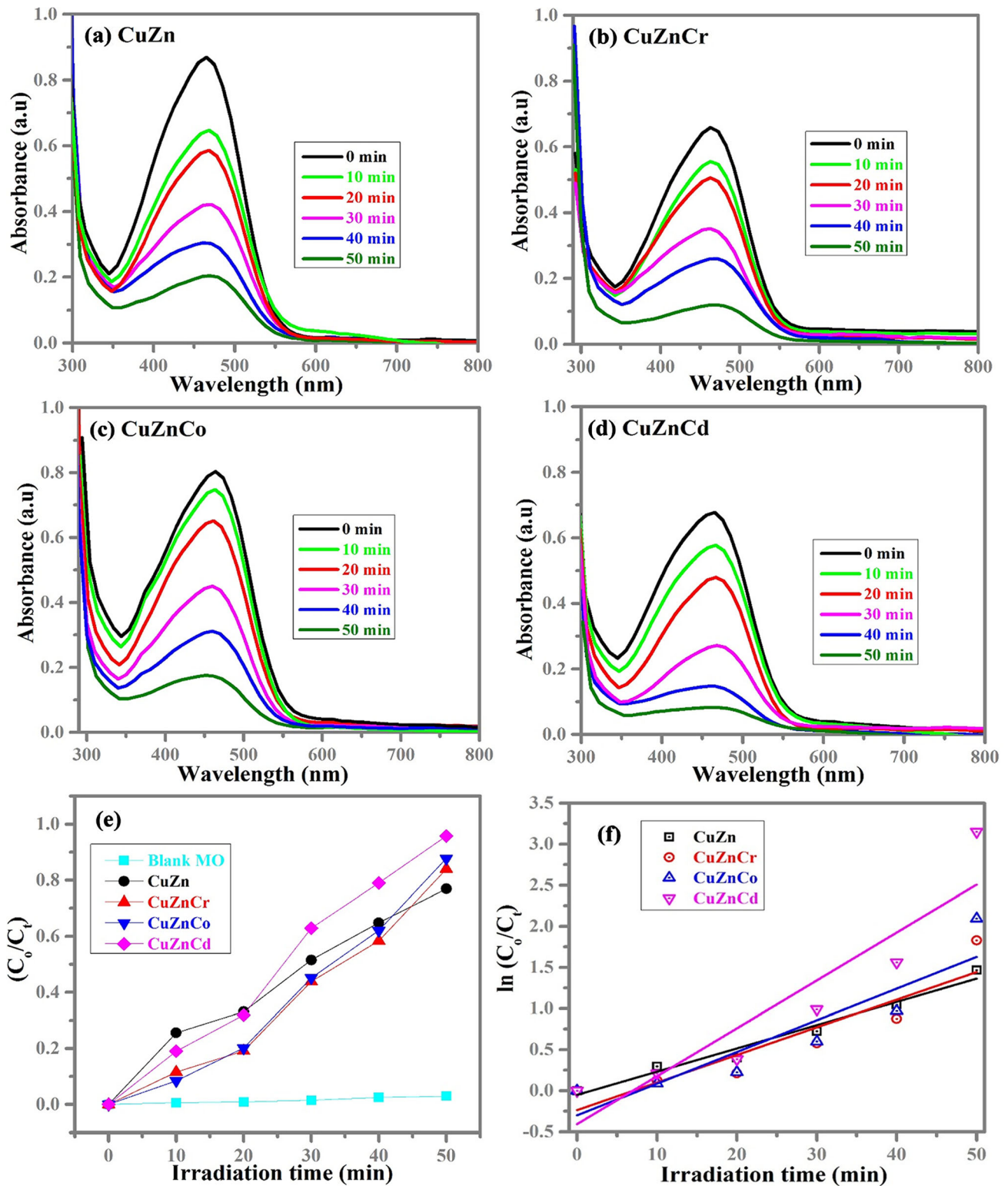
Fig. 9 Absorption spectra of methyl orange (MO) dye in the presence of **a** CuZn, **b** CuZnCr, **c** CuZnCo, **d** CuZnCd photocatalyst, **e** % age degradation, and **f** kinetic plot for rate constant (k)

$$k = 17/l^3 \quad (11)$$

$$c = \lambda v_o = v_o/\overline{v} \quad (12)$$

$$hv_o = k_B \theta_D \quad (13)$$

where k_B and h are Boltzmann and Planck's constant, respectively. The calculated values are summarized in Table 3. Furthermore, the obtained results of bond length (l) are in good agreement with values calculated by XRD.

3.3 Optical analysis

Studying the optical characteristics of grown samples is necessary for their aptness in optical applications, especially for photocatalytic activity. For optical measurements, the grown samples are initially dispersed in absolute ethanol and sonicated for 30 min, and then absorption spectra are trace between 400 and 1250 nm. The absorption and transmission spectra of CuZn, CuZnCr, CuZnCo, and CuZnCd nanocrystals are presented in Fig. 4. The CuZn nanocrystal has an absorption peak at 1016 nm and co-doped CuZnCr, CuZnCo, and CuZnCd nanocrystals at 1046, 1046, and 1057 nm, respectively. Contrary, the transmittance spectra of the as-synthesized samples have opposite behavior than absorption spectra, as shown in Fig. 4b.

3.4 Optical energy bandgap

The direct energy bandgap of the as-obtained products is determined using Tauc's relation as [57, 58]

$$\alpha hv = A(hv - E_g)^n \quad (14)$$

where α, h, A, v, E_g, and n are the absorption coefficient, Planck's constant, band tailing parameter, light frequency, energy gap, and power factor of transition mode, respectively. The E_g is calculated by plotting $(\alpha hv)^2$ against hv and extrapolating the linear part on the energy axis up to zero (Fig. 5). The direct energy gap 1.260, 1.197, 1.182, and 1.181 eV for CuZn, CuZnCr, CuZnCo, and CuZnCd nanocrystals, respectively, is obtained for grown nanocrystals. The energy bandgap is decreased as the crystallite size is increased, also the structural deformation (evident from XRD Sect. 3.1), is occurred by incorporation/substitution of dopants ions into host CuO matrix. Consequently, these dopants ions would create additional energy levels below the conduction band or above the valance band in the CuO bandgap and may cause a reduction in direct transition energy. Kuldeep Kumar et al. [59] also reported similar kind of reduction in energy bandgap of CuO by Ag/Co co-doping.

3.5 Current–voltage (I–V) measurements

I–V curves between applied voltage (− 5 to 5 V) and current (I) at room temperature for grown products are displayed in Fig. 6. The as-synthesized nanocrystals have ohmic nature [60], can be perceived from Fig. 6. The co-doped (CuZnCr, CuZnCo, and CuZnCd) nanocrystals have a higher value of current at terminal voltage, which suggested that the electrical conductivity of co-doped CuO is higher than single (Zn)-doped CuO.

Table 4 Photodegradation kinetic parameters

| Equation $y = a + b \times x$					
	Intercept	Slope	Residual sum of squares	Pearson's r	Adj. R-square
MB dye					
CuZn	− 0.21385	0.04797	0.16693	0.97990	0.95025
CuZnCr	− 0.51970	0.06181	2.13202	0.87075	0.69777
CuZnCo	− 0.43483	0.06717	1.55303	0.91413	0.79453
CuZnCd	− 0.43531	0.07431	1.58387	0.92692	0.82397
MO dye					
CuZn	− 0.05170	0.02829	0.03666	0.98717	0.96813
CuZnCr	− 0.23743	0.03361	0.34509	0.92270	0.81422
CuZnCo	− 0.30076	0.03857	0.50868	0.91462	0.79566
CuZnCd	− 0.40798	0.05830	0.97546	0.92688	0.82388
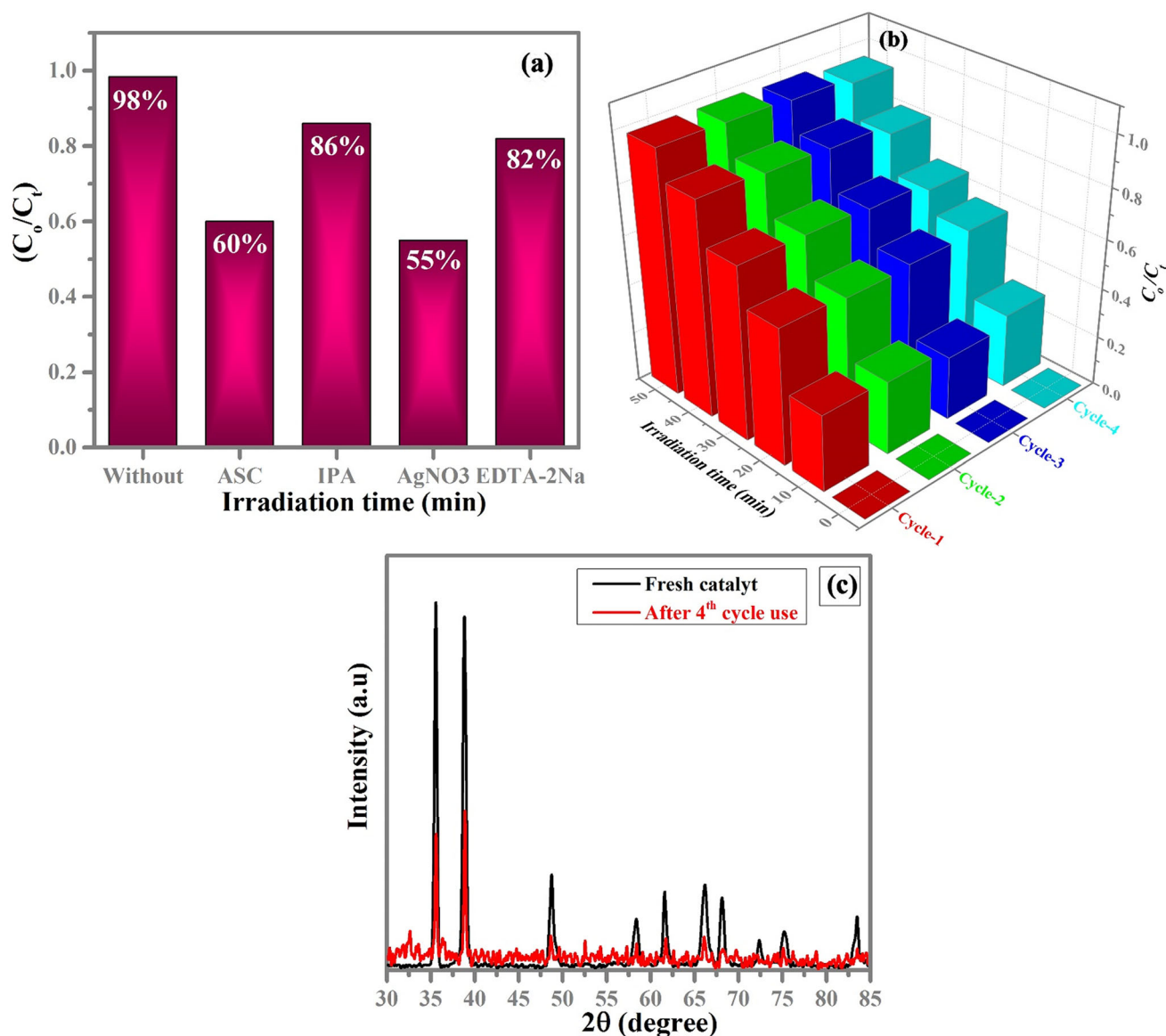
Fig. 10 **a** Degradation efficiency (%) by adding different scavengers, **b** recyclability test profile, in the presence of CuZnCd catalyst against MB dye, and **c** XRD spectra before and after reusability

3.6 SEM analysis

Figure 7a–d illustrates the SEM images of CuZn, CuZnCr, CuZnCo, and CuZnCd nanocrystals, respectively. The accumulation of several metal ions altered the morphology, as shown in Fig. 7. The SEM images showed the highly agglomerated morphology.

3.7 Photocatalytic activity

The photocatalytic characteristics of the as-obtained nanocrystals are investigated against the photodegradation of MB and MO dyes under direct sunlight irradiation. The absorption spectra of the MB dye solution at varying time intervals are shown in Fig. 8a–d and MO dye are shown in Fig. 9a–d. The % degradation of CuZn, CuZnCr, CuZnCo, and CuZnCd nanocrystals after 50 min sunlight illumination against MB dye was 91.2%, 97.1%, 97.7%, and 98.4%, respectively, (Fig. 8e) and against MO dye was 77.0%, 84.0%, 87.0% and 96.1%, respectively (Fig. 9e). The CuZnCd catalyst has shown remarkably higher decolorization efficiency for MB and MO than other nanocrystals. The difference in the degradation efficiency is attributed due to the dissimilar nature or

Table 5 Comparison of decolorization efficiency (%) of grown nanocrystals with some other doped CuO materials

Photocatalysts	Dyes	Efficiency (%)	Refs
Ag/CuO	MB	86.0	[63]
Zn-doped CuO	–	90.43	[64]
Mn-doped CuO	–	87.0	[65]
Zn/Ag-CuO	–	78.0	[66]
Co-doped CuO	–	82.32	[67]
Fe, Co co-doped CuO	–	94.9	[27]
CuZn	–	92.2	Present
CuZnCr	–	97.1	Present
CuZnCo	–	97.7	Present
CuZnCd	–	98.4	Present
Ag, Co co-doped CuO	MO	87.0	[68]
Fe/Co-ZnO	–	95.30	[69] Previous
CuZn	–	77.0	Present
CuZnCr	–	84.0	Present
CuZnCo	–	87.0	Present
CuZnCd	–	96.1	Present

molecular structure of dyes. The photocatalytic performance of prepared photocatalyst is explained by kinetic studies using the pseudo-first-order kinetic model [61, 62]:

$$C_t = C_o e^{-kt} => \ln(C_o/C_t) = kt \tag{15}$$

Here, k is the first-order rate constant. Plotting term $ln(C_o/C_t)$ versus irradiation time (Figs. 8f and 9f), the slope gives the value of k. The value of k for CuZn, CuZnCr, CuZnCo, and CuZnCd nanocrystals were 0.04797, 0.06181, 0.06717, and 0.07431 min^{-1} for the degradation of MB dye and 0.02829, 0.03361, 0.03857, and 0.0583 min^{-1} for the degradation of MO dye, respectively. Further, Adj. R-Square, Residual Sum of Squares, and Pearson's r values were calculated and are provided in Table 4 to strengthen the linear association of given data. The photodegradation test of blank MB and MO dyes in the absence of catalysts were also carried out (Figs. 8, 9e) under sunlight, which exhibits not any noticeable amount of dyes degradation. The comparison of photodegradation efficiency of grown catalysts with some other reports is provided in Table 4. The improvement in photocatalytic performance was due to the following factors: First, the decrease in energy gap by co-doping can support the excitation of extra electrons from *VB* to *CB* with comparatively low energy and excess of electrons in the *CB*. Second, the intermediate states

are generated by co-doping within the bandgap, which allows the trapping of electrons and increases the charge separation and hinders the recombination of charge carriers. Furthermore, the scavengers test exhibits that the photodegradation is quenched by adding reactive species AgNO$_3$, isopropanol (IPA), EDTA-2Na, and ASC with efficiencies 55%, 86%, 82%, and 60%, respectively (Fig. 10a), as compared to blank catalyst test (without scavengers) 98.4%. The results evidenced the major role of electrons and superoxide radicals are in the photodegradation reaction. As the durable reusability and stability of the catalyst is an essential factor for more practical application to the elimination of organic pollutants from the contaminant water. The recyclability test was performed using the CuZnCd catalyst having maximum degradation against MB dye. The results exhibit only a small decrement in photodegradation efficiency from 98.4 to 96.66% after the fourth cycle of use (Fig. 10b). The structural changes in the catalyst after the reusability test was investigated by taking again XRD spectra (Fig. 10c), which shows that there is no significant change occur after the fourth cycle of reuse.

3.8 Antibacterial activities

Different bacteria, including *Klebsiella pneumoniae* and *Staphylococcus aureus,* are selected to test the antibacterial activity of synthesized CuZn, CuZnCr, CuZnCo, and CuZnCd nanocrystals at different concentrations. The observed values for ZOI using prepared nanocrystals along with antibiotic Ciprofloxacin (standard values) are listed in Table 5 and presented in Figs. 11 and 12, respectively. It is well known from the literature that if ZOI diameter is ≥ 6 mm, then the material possesses good antibacterial property, and if ZOI is not in this range, the material has deprived antibacterial activity. Moreover, oxides of metal are good antibacterial agents. The results of the current study indicate that better antibacterial activity can be achieved by using co-doped nanocrystals, and it is also important to mention here that ZOI is greater for all nanocrystals from the threshold value. The ZOI is shown in (Figs. 11, 12) against bacterial strains, clearly indicates that our grown antibacterial agent is useful against pathogen bacteria. The comparison of antibacterial activity of grown catalysts with some other oxide materials is provided in Table 6.
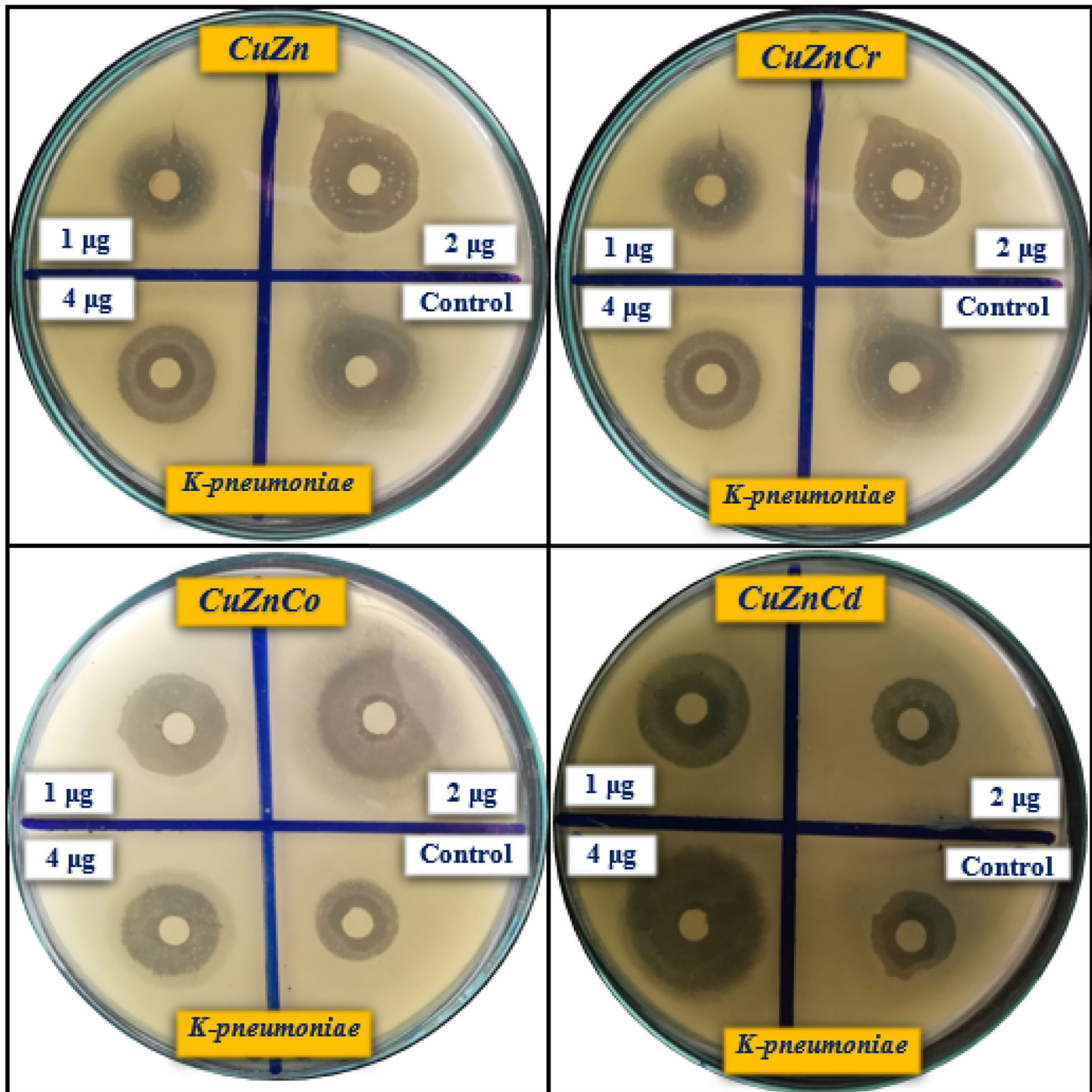
Fig. 11 Antibacterial activity of CuZn, CuZnCr, CuZnCo, and CuZnCd along with standard antibiotics Ciprofloxacin gram-negative *Klebsiella Pneumoniae* bacteria

The antibacterial characteristics of co-doped CuO nanocrystals can be illustrated in the following facts. The size of nanocrystals lies within the nanometers, which is comparable with the size of the bacteria, so these particles can easily penetrate in bacteria, resulting in damage to the bacteria cell. The shape and surface area of the material are also dominant in antibacterial activity because the rough surface can mechanically damage the bacteria, the higher surface area is responsible for greater production of ROS species. The ROS species can destruct DNA or protein cells by creating highly reactive O_2^{*-} radicals. Furthermore, it is also assumed that the death of cells occurs due to the interaction of bacteria (negative charge) and nanoparticles (positive charge). The comparison of antibacterial activity of grown
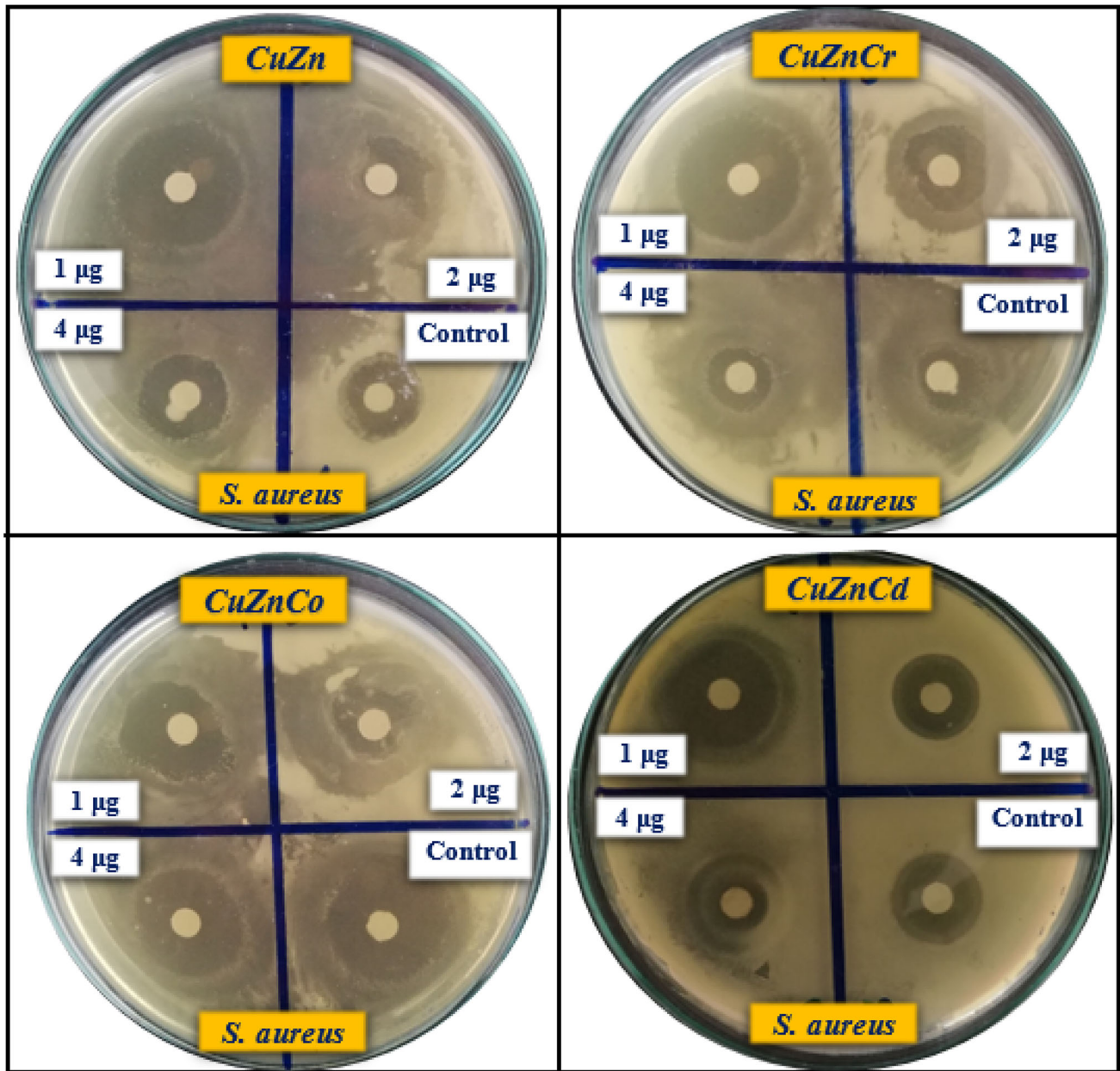
Fig. 12 Antibacterial activity of CuZn, CuZnCr, CuZnCo, and CuZnCd along with standard antibiotics Ciprofloxacin gram-positive *Staphylococcus aureus* bacteria

Table 6 Antimicrobial activity of grown nanocrystals at concentrations

Composition	Zone of (mm) for *S. aureus*				ZOI (mm) for *K-pneumoniae*			
	1 µg	2 µg	4 µg	Control	1 µg	2 µg	4 µg	Control
CuZn	25	12	14	15	29	28	27	20
CuZnCr	21	24	12	15	24	22	23	21
CuZnCo	25	29	31	19	21	27	22	23
CuZnCd	25	22	27	19	32	18	22	17

Table 7 The comparison of antibacterial activity of grown nanocrystals with some other pure and doped metal oxides

Bacteria	Materials	Zone of inhibition (mm)	References
S. aureus	CuAgNiO	13	[70]
	Fe/Cd co-doped ZnO	14	[71]
	Cu/Ag	14	[72]
	CuO	12.4	[73]
	CuO	26.50	[74]
	MgCrNiO	25	Previous [75]
	ZnCeVO	14	Previous [41]
	ZnLaSmO	13	Previous [76]
	CuZnCo	31	Present
K-pneumoniae	ZnO:Nd	14	[77]
	CuO	28.75	[74]
	CuO	27	[19]
	Fe/Co-ZnO	25	Previous [69]
	CuZnCd	32	Present

nanocrystals with some other pure and doped metal oxides is provided in Table 7.

4 Conclusion

In summary, $Cu_{0.95}Zn_{0.05}O$ and $Cu_{0.9}Zn_{0.05}M_{0.05}O$ (M = Cr, Co, Cd) nanocrystals were prepared by sol–gel method. XRD results exhibit that TM ions (Zn, Cr, Co, or Cd) were successfully incorporated in CuO matrix. The lattice parameter varied according to the ionic radii of dopants. The X-ray peak profile analysis has confirmed the presence of tensile strain. The direct energy bandgap was red-shifted from 1.26 to 1.81 eV by co-doping. The I–V measurements have confirmed the enhancement in the electrical properties by the co-doping. The photocatalytic test for removal of MB and MO dyes under direct sunlight has shown that co-doping has significantly improved the photocatalytic properties of CuO, with Zn + Cd-doped nanocrystal has a higher degradation 98.4% against MB and 96.1% against MO dye in 50 min. The major role of reactive species (electrons and superoxide radical) in degradation reaction is confirmed by scavenger test. The antibacterial property was studied against *Staphylococcus aureus* and *Klebsiella pneumoniae* bacterial strains and Zn/Cd-doped nanocrystal has exhibited the highest activity against *S. aureus* and Zn/Co-doped nanocrystal showed the highest activity against *K. pneumoniae* bacteria. Furthermore, the present article imparts an idea to improve the existing properties of CuO by structural variation with TM co-doping for environmental and biomedical applications.

References

1. S. Zinatloo-Ajabshir, N. Ghasemian, M. Mousavi-Kamazani, M. Salavati-Niasari, Ultrason. Sonochem. **71**, 105376 (2021)
2. S. Zinatloo-Ajabshir, M. Mousavi-Kamazani, Ceram. Int. **46**, 26548 (2020)
3. M. Arunpandian, K. Selvakumar, A. Raja, P. Rajasekaran, M. Thiruppathi, E.R. Nagarajan, S. Arunachalam, Colloids Surf. A Physicochem. Eng. Asp. **567**, 213 (2019)
4. K. Qi, B. Cheng, J. Yu, W. Ho, J. Alloys Compd. **727**, 792 (2017)
5. M. Faraz, F.K. Naqvi, M. Shakir, N. Khare, New J. Chem. **42**, 2295 (2018)
6. S. Xia, L. Zhang, G. Pan, P. Qian, Z. Ni, Phys. Chem. Chem. Phys. **17**, 5345 (2015)
7. R. Bomila, S. Srinivasan, S. Gunasekaran, A. Manikandan, J. Supercond. Nov. Magn. **31**, 855 (2018)
8. A. Meng, J. Xing, Z. Li, Q. Li, ACS Appl Mater. Interfaces **7**, 27449 (2015)
9. U. Alam, RSC Adv. **8**, 17582 (2018)
10. J. You, Y. Guo, R. Guo, X. Liu, Chem. Eng. J. **373**, 624 (2019)
11. Q. Liu, E. Liu, J. Li, Y. Qiu, R. Chen, Catal. Today **339**, 391 (2020)

12. T. Munawar, F. Mukhtar, M.S. Nadeem, K. Mahmood, A. Hussain, A. Ali, M.I. Arshad, M. Ajazun-Nabi, F. Iqbal, Solid State Sci. **106**, 106307 (2020)

13. T. Munawar, F. Mukhtar, M.S. Nadeem, K. Mahmood, M. Hasan, A. Hussain, A. Ali, M.I. Arshad, F. Iqbal, Mater. Chem. Phys. **253**, 123249 (2020)

14. T. Munawar, F. Mukhtar, M.S. Nadeem, M. Asghar, K. Mahmood, A. Hussain, M.I. Arshad, M. Ajaz, F. Iqbal, Ceram. Int. **46**, 22345 (2020)

15. X. Yu, T.J. Marks, A. Facchetti, Nat. Mater. **15**, 383 (2016)

16. M.S. Chavali, M.P. Nikolova, SN Appl. Sci. **1**, 1 (2019)

17. S. Anitha, M. Suganya, D. Prabha, J. Srivind, S. Balamurugan, A.R. Balu, Mater. Chem. Phys. **211**, 88 (2018)

18. A.O. Juma, E.A.A. Arbab, C.M. Muiva, L.M. Lepodise, J. Alloys Compd. **723**, 866 (2017)

19. H.C. Ananda Murthy, B. Abebe, C.H. Prakash, K. Shantaveerayya, Mater. Sci. Res. India **15**, 279 (2018)

20. T.H. Tran, V.T. Nguyen, Int. Sch. Res. Not. **2014**, 1 (2014)

21. S. Jillani, M. Jelani, N.U. Hassan, S. Ahmad, M. Hafeez, Mater. Res. Express **5**, 045006 (2018)

22. M. Rafique, A.J. Shaikh, R. Rasheed, M.B. Tahir, H.F. Bakhat, M.S. Rafique, F. Rabbani, NANO **12**, 1750043 (2017)

23. U.T. Khatoon, K. Mohan Mantravadi, G.V.S. Nageswara Rao, Mater. Sci. Technol. (United Kingdom) **34**, 2214 (2018)

24. A.P. Nagvenkar, A. Gedanken, ACS Appl. Mater. Interfaces **8**, 22301 (2016)

25. N. Thakur, J. Kumar, Int. J. Adv. Res. Sci. Eng. **7**, 2319 (2018)

26. X. Xiong, C. You, Z. Liu, A.M. Asiri, X. Sun, ACS Sustain. Chem. Eng. **6**, 2883 (2018)

27. A.M. El-Sayed, M. Shaban, Spectrochim. Acta Part A Mol. Biomol. Spectrosc. **149**, 638 (2015)

28. M. Shaban, K. Abdelkarem, A.M. El-Sayed, Phase Trans. **92**, 347 (2019)

29. J.A. Hence Sheela, S. Lakshmanan, A. Manikandan, S. Arul Antony, J. Inorg. Organomet. Polym. Mater. **28**, 2388 (2018)

30. C. Amirthavalli, A. Manikandan, A.A.M. Prince, Ceram. Int. **44**, 15290 (2018)

31. A. Manikandan, J.J. Vijaya, C. Ragupathi, L.J. Kennedy, J. Nanosci. Nanotechnol. **14**, 2584 (2014)

32. A. Manikandan, J.J. Vijaya, S. Narayanan, L.J. Kennedy, J. Nanosci. Nanotechnol. **14**, 2507 (2014)

33. L. Dörner, C. Cancellieri, B. Rheingans, M. Walter, R. Kägi, P. Schmutz, M.V. Kovalenko, L.P.H. Jeurgens, Sci. Rep. **9**, 1 (2019)

34. T. Munawar, S. Yasmeen, M. Hasan, K. Mahmood, A. Hussain, A. Ali, M.I. Arshad, F. Iqbal, Ceram. Int. **46**, 11101 (2020)

35. T. Munawar, F. Mukhtar, M.S. Nadeem, M. Riaz, M.N. Rahman, K. Mahmood, M. Hasan, M.I. Arshad, F. Hussain, A. Hussain, F. Iqbal, Solid State Sci. **109**, 106446 (2020)

36. D. Saravanakkumar, S. Sivaranjani, K. Kaviyarasu, A. Ayeshamariam, B. Ravikumar, S. Pandiarajan, C. Veeralakshmi, M. Jayachandran, M. Maaza, J. Semicond. **39**, 033001 (2018)

37. T. Munawar, S. Yasmeen, F. Hussain, K. Mahmood, A. Hussain, M. Asghar, F. Iqbal, Mater. Chem. Phys. **249**, 122983 (2020)

38. S. Yasmeen, F. Iqbal, T. Munawar, M.A. Nawaz, M. Asghar, A. Hussain, Ceram. Int. **45**, 17859 (2019)

39. T. Munawar, F. Iqbal, S. Yasmeen, K. Mahmood, A. Hussain, Ceram. Int. **46**, 2421 (2020)

40. S. Yasmeen, T. Munawar, M. Asghar, M.A. Khan, A. Hussain, F. Iqbal, J. Mater. Res. Technol. **9**, 4096 (2020)

41. T. Munawar, S. Yasmeen, F. Mukhtar, M.S. Nadeem, K. Mahmood, M. Saqib-Saif, M. Hasan, A. Ali, F. Hussain, F. Iqbal, Ceram. Int. **46**, 14369 (2020)

42. S. Dong, X. Zhang, S. Dong, X. Zhou, L. Yan, G. Chen, D. Zhou, Mater. Lett. **143**, 312 (2015)

43. A.N. Ökte, Appl. Catal. A Gen. **475**, 27 (2014)

44. S. Anandan, S. Muthukumaran, Opt. Mater. (Amst). **35**, 2241 (2013)

45. C. Belkhaoui, N. Mzabi, H. Smaoui, P. Daniel, Results Phys. **12**, 1686 (2019)

46. M.S. Nadeem, T. Munawar, F. Mukhtar, M. Naveed, M. Riaz, A. Hussain, F. Iqbal, Opt. Mater. (Amst) (2020). https://doi.org/10.1016/j.ceramint.2021.03.173

47. S.N. Anitha, I. Jayakumar, J. Nanosci. Technol. **1**, 26 (2015)

48. M. Kahouli, A. Barhoumi, A. Bouzid, A. Al-hairy, S. Guermazi, Superlattices Microstruct. **85**, 7 (2015)

49. S. Moshtaghi, S. Zinatloo-Ajabshir, M. Salavati-Niasari, J. Mater. Sci. Mater. Electron. **27**, 425 (2016)

50. S. Anand, A.P. Amaliya, M.A. Janifer, S. Pauline, Mod. Electron. Mater. **3**, 168 (2017)

51. R. Sivakami, S. Dhanuskodi, Spectrochim. Acta Part A **152**, 43 (2016)

52. Z.N. Kayani, M. Umer, S. Riaz, S. Naseem, J. Electron. Mater. **44**, 3704 (2015)

53. E.P. Etape, L.J. Ngolui, J. Foba-tendo, D.M. Yufanyi, B.V. Namondo, J. Appl. Chem. **2017**, 1 (2017)

54. M. Sathya, K. Pushpanathan, Appl. Surf. Sci. **449**, 346 (2018)

55. H. Singh, K.L. Yadav, Ceram. Int. **41**, 9285 (2015)

56. M.M. El-Desoky, M.A. Ali, G. Afifi, H. Imam, M.S. Al-Assiri, SILICON **10**, 301 (2018)

57. J. Al Boukhari, L. Zeidan, A. Khalaf, R. Awad, Chem. Phys. **516**, 116 (2019)

58. A.S. Hassanien, A.A. Akl, Superlattices Microstruct. **89**, 153 (2016)

59. N. Thakur, K. Kumar, J. Environ. Chem. Eng. **8**, 1 (2020)

60. M.L. Dinesha, H.S. Jayanna, S. Mohanty, S. Ravi, J. Alloys Compd. **490**, 618 (2010)

61. T. Munawar, S. Yasmeen, A. Hussain, M. Akram, F. Iqbal, Mater. Lett. **264**, 127357 (2020)

62. F. Mukhtar, T. Munawar, M. Shahid, N. Murtaza, H. Fayyaz, Appl. Phys. A **126**, 1 (2020)

63. M.U. Khalid, M.F. Warsi, M.I. Sarwar, P.O. Agboola, I. Shakir, S. Zulfiqar, Ceram. Int. **46**, 14287 (2020)

64. T. Jiang, Y. Wang, D. Meng, D. Wang, J. Mater. Sci. Mater. Electron. **27**, 12884 (2016)

65. T. Jiang, J. Kong, Y. Wang, D. Meng, D. Wang, M. Yu, Cryst. Res. Technol. **51**, 58 (2016)

66. N.F. Andrade Neto, P.M. Oliveira, C.A. Paskocimas, M.R.D. Bomio, F.V. Motta, J. Electron. Mater. **48**, 4840 (2019)

67. A. Pramothkumar, N. Senthilkumar, K.C.M. Gnana Malar, M. Meena, I. Vetha Potheher, J. Mater. Sci. Mater. Electron. **30**, 19043 (2019)

68. E.F.A. Zeid, I.A. Ibrahim, W.A.A. Mohamed, A.M. Ali, Mater. Res. Express **7**, 026201 (2020)

69. M.S. Nadeem, T. Munawar, F. Mukhtar, M.N. Rahman, M. Riaz, F. Iqbal, Ceram. Int. (2020). https://doi.org/10.1016/j.ceramint.2021.03.173

70. N. Thakur, K. Kumar, K.K. Sharma, Inorg. Nano-Metal Chem. **50**, 933 (2020)

71. D. Neena, K.K. Kondamareddy, H. Bin, D. Lu, P. Kumar, Sci. Rep. **8**, 1 (2018)

72. R.B. Asamoah, E. Annan, B. Mensah, P. Nbelayim, V. Apalangya, B. Onwona-Agyeman, A. Yaya, Adv. Mater. Sci. Eng. **13**, 17 (2020)

73. S. Moniri Javadhesari, S. Alipour, S. Mohammadnejad, M.R. Akbarpour, Mater. Sci. Eng. C **105**, 110011 (2019)

74. L.M. Dwivedi, N. Shukla, K. Baranwal, S. Gupta, S. Siddique, V. Singh, J. Clust. Sci. **32**, 209 (2021)

75. T. Munawar, M.S. Nadeem, F. Mukhtar, A. Azhar, M. Hasan, K. Mahmood, A. Hussain, A. Ali, M.I. Arshad, M. Ajaz Nabi, F. Iqbal, Phys. B Condens. Matter **602**, 412555 (2020)

76. T. Munawar, M.S. Nadeem, F. Mukhtar, M. Hasan, K. Mahmood, M.I. Arshad, A. Hussain, A. Ali, M.S. Saif, F. Iqbal, Mater. Sci. Semicond. Process. **122**, 105485 (2021)

77. A.S.H. Hameed, C. Karthikeyan, A.P. Ahamed, N. Thajuddin, N.S. Alharbi, S.A. Alharbi, G. Ravi, Sci. Rep. **6**, 1 (2016)